



# Creep flow, diffusion, and electromigration in small scale interconnects

Dongchoul Kim, Wei Lu\*

*Department of Mechanical Engineering, University of Michigan, Ann Arbor, MI 48109, USA*

Received 2 November 2005; received in revised form 30 May 2006; accepted 6 June 2006

---

## Abstract

This paper proposes a three-dimensional electromigration model for void evolution in small scale interconnects. Concurrent kinetics of creep flow and surface diffusion as well as the effect of the surrounding material is considered to provide better understanding of the evolution process. The multiple kinetics and energetics are incorporated into a diffusive interface model. A semi-implicit Fourier spectral method and the preconditioned biconjugate-gradient method are proposed for the computations to achieve high efficiency and numerical stability. We systematically studied kinetic processes in diffusion dominated to creep dominated regime. Which process dominates, as revealed by the analysis, is determined by a combination of viscosity, mobility, interconnect thickness, and void radius. Previous studies on electromigration suggest that a circular void subjected to an electron wind force and surface diffusion is always stable against any small shape perturbation. Our simulations show that a shape that is stable in surface diffusion can become unstable in a creep dominated process, which leads to a quite different void morphology. A spherical void can evolve into a bowl shape and further break into smaller voids. It is also shown that the interconnect geometry has an important effect.

© 2006 Elsevier Ltd. All rights reserved.

*Keywords:* Electromigration; Creep; Nanostructure; Phase field model

---

---

\*Corresponding author. Tel.: +1 734 647 7858; fax: +1 734 647 3170.  
*E-mail address:* [weilu@umich.edu](mailto:weilu@umich.edu) (W. Lu).

## 1. Introduction

Void evolution in interconnects induced by electromigration has significant effect on the reliability of integrated circuits. Interconnects are thin wires of copper or aluminum alloy which make electrical contact between devices on a chip. The continuous scaling down in the dimensions of typical integrated circuits leads to increasing electric current densities in interconnect lines. As a result, current induced directional mass transport causes nucleation of voids. Nucleated voids in interconnects change their shape and sometimes cause an open circuit as a result of the small dimensions, intense currents, and elevated temperatures. This phenomenon has largely limited further device miniaturization and needs to be addressed.

Many theoretical studies have contributed to the understanding of void morphological evolution and its implication for electromigration induced failure (Bhate et al., 2000; Cho et al., 2004; Fridline and Bower, 1999; Gungor and Maroudas, 1998, 1999; Wang et al., 1996). The electron wind promotes the formation of slits while the surface energy favors rounded voids. A spherical void becomes unstable in a large electric current. Depending on the initial shape a void may elongate in the direction normal to or along the interconnect line (Wang et al., 1996). Fridline and Bower (1999) studied the effect of anisotropic surface diffusivity on the formation and growth of slit-like voids. They modeled an interconnect as a two-dimensional electrically conducting strip containing an initially semi-circular void. Finite element computation was applied to predict void evolution. Gungor and Maroudas considered electromigration-induced failure due to transgranular void propagation (Cho et al., 2004; Gungor and Maroudas, 1998, 1999). Bhate et al. (2000) investigated stress-induced void evolution in interconnects with a phase field model.

While diffusion has been investigated as a mass transport mechanism in electromigration, recent studies suggest that creep can play an important role. Bower and Freund considered creep deformation by dislocation and sliding motion at grain boundaries and the interface between the interconnect and passivation (Bower and Freund, 1993; Fridline and Bower, 2002). They investigated voids initially nucleated and grown at the grain boundary, and showed that the inelastic slip between the interconnect and the surrounding passivation plays a central role in developing a narrow slit or a round shape. Although in this work the driving force for diffusion and creep was thermal residual stress rather than electromigration, the study highlighted the importance of the creep mechanism in void evolution. When creep occurs in grains and diffusion occurs on grain boundaries there is no ambiguity about their distinct contributions. However, creep and diffusion occur in the same continuum space when we consider. Suo (2004) theoretically considered the coupled effect in a single-component material. Both convection and diffusion contributed to mass transport. Convection was identified by the motion of imaginary markers dispersed in the material. Creep and diffusion coupled because the markers must move to compensate for the diffusion flux divergence. The Stokes equation and Herring model were adopted to describe creep and diffusion, respectively. Experimentally, the effect of creep flow was demonstrated in electromigration-induced hillocking (Glickman et al., 1997; Proost et al., 2002).

This paper studies void evolution driven by electromigration in a small scale interconnect. The high electric current density induces high temperature, high-pressure gradients and low viscosity, where creep flow has a significant effect. A study considering concurrent kinetics and small interconnect size is necessary to respond to the new demands

of nanoscale devices. When the size of an interconnect is reduced below the grain size, the grain boundaries no longer connect into a continuous diffusion path. Thus we focus on the void evolution process inside the grain rather than at the grain boundary. In fact, slit voids were commonly observed inside grains even in a micro-scale interconnect (Arzt et al., 1994; Kraft and Arzt, 1997). We aim to reveal the dynamic void evolution process in interconnects by studying the interplay of the electron wind, surface energy, surface diffusion and creep. A three-dimensional model capable of describing the rich dynamics is developed in this paper, which can provide more realistic simulations beyond existing two-dimensional diffusion models. To overcome the computational complexity due to evolving interfaces, multiple energetics and kinetics, a diffuse interface approach is adopted. Similar approaches have been applied in previous studies and demonstrated its reliability and effectiveness (Kim and Lu, 2004; Lu and Kim, 2004; Lu and Salac, 2005). In contrast to interface tracking methods such as the boundary element method, the interfaces are not modeled explicitly but given implicitly by a concentration field, where an interface is represented by a thin continuous transition region. Consequently, complex interface changes, such as void breaking or coalescence, will not cause any additional computational difficulty.

## 2. A diffuse interface model for coupled diffusion and creep flow

Interconnects in current devices are made of aluminum or copper alloys, and are typically of a rectangular cross-section with dimensions in the submicron range. They are deposited on a silicon substrate and then encapsulated in a thick oxide layer. The encapsulation of aluminum lines by insulating layers eliminates atomic sinks such as hillocks. Fig. 1 shows an interconnect line subjected to an electric field. The material surrounding the line is assumed to be much stiffer than aluminum. We consider the migration and morphological evolution of a small void that has already nucleated, as shown in Fig. 1. A coordinate system is attached so that the  $x_1$ – $x_2$  plane coincides with the bottom of the interconnect line. Define a concentration  $C$  by the volume fraction of metal,  $C = 0$  for void and  $C = 1$  for metal. Regard the concentration as a spatially continuous and time-dependent function  $C(x_1, x_2, x_3, t)$ . We consider regions away from any possible grain boundary in the metal line (such as the bamboo structure) so that the only mass transport mechanism is surface diffusion and creep flow. For simplicity, we assume isotropic surface energy and diffusivity.

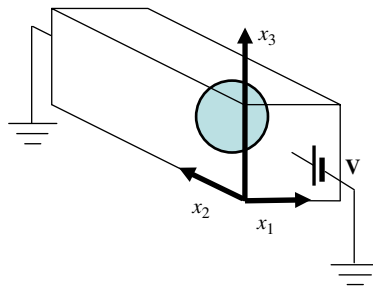


Fig. 1. An illustration of a void in a thin interconnect line subjected to an electric field. The electric current flows in  $x_1$  direction.

### 2.1. Electron wind

The metal lines or interconnects in today's integrated circuits are subject to high current density due to continuing miniaturization. For instance, the current density in an aluminum interconnect can reach  $10^{10}$  A/m<sup>2</sup>. The electron wind exerts a force,  $\mathbf{F}_e$ , in the direction of the electron flow at the void surface. The force on a per unit volume basis is given by (Wang et al., 1996).

$$\mathbf{F}_e = -N_a Z^* |e| \mathbf{E}, \quad (2.1)$$

where  $N_a$  is the number of atoms per unit volume,  $Z^*$  the phenomenological effective valence of the atom and  $e$  the charge of an electron. The negative sign in Eq. (2.1) means that the force is in the direction of the electron flow. The electric field,  $\mathbf{E}$ , relates to the electric potential,  $\phi$ , by

$$\mathbf{E} = -\nabla\phi. \quad (2.2)$$

Conservation of electric charges requires that a steady electric current density,  $\mathbf{j}$ , satisfies

$$\nabla \cdot \mathbf{j} = 0. \quad (2.3)$$

The electric field relates to the current density by Ohm's law, namely

$$\mathbf{j} = \sigma \mathbf{E}, \quad (2.4)$$

where  $\sigma$  is the conductivity of the media. The electric field inside the void is much lower than the electric breakdown strength of vacuum or dry air. Therefore the void can be modeled as an insulator. Denote the conductivity of the metal by  $\sigma_0$ . We interpolate the electric conductivity linearly by the values of metal and the void, namely,  $\sigma(C) = \sigma_0 C$ . A combination of Eqs. (2.1)–(2.4) shows that the electric potential obeys the Laplace equation:

$$\nabla \cdot \{\sigma(C) \nabla \phi\} = 0. \quad (2.5)$$

This partial differential equation, together with boundary conditions, determines the electric potential.

### 2.2. Surface diffusion

Atoms diffuse on a void surface from high chemical potential regions to low chemical potential regions, which causes the void to change its shape or drift along the metal line. The diffusion driving force relates to the chemical potential,  $\mu_0$ , by  $\mathbf{F}_c = -\nabla\mu_0$ . The electron wind provides an additional driving force as shown in Eq. (2.1). The total driving force can be expressed by  $\mathbf{F} = \mathbf{F}_c + \mathbf{F}_e$ , which leads to a mass flux of

$$\mathbf{J} = -M(\nabla\mu_0 - N_a |e| Z^* \nabla\phi), \quad (2.6)$$

where  $M$  is the mobility. The bulk diffusion can be neglected since the surface diffusion on the void surface is much faster. To consider surface diffusion, we take  $M$  to have the form of  $M(C) = M_0 C(1 - C)$ , where  $M_0$  is a material constant. Note that  $M(C)$  vanishes outside the interfacial region.

The chemical potential relates to the free energy,  $G$ , by  $\mu_0 = \delta G / \delta C$ . The expression of  $G$  is standard in the Cahn–Hilliard model (Cahn, 1958), which is

$$G = \int_V \left( g(C) + \frac{1}{2} h |\nabla C|^2 \right) dV. \quad (2.7)$$

The first term in Eq. (2.7) represents the chemical energy that drives phase separation; it can be any function with double wells. We use  $g(C) = f_0 C^2 (1 - C)^2$ , where  $f_0$  is a positive constant. The second term of Eq. (2.7) accounts for the interface energy between void and metal, where  $h$  is a material constant. These give  $\mu_0 = f_0 (4C^3 - 6C^2 + 2C) - h \nabla^2 C$ .

### 2.3. Creep

Both Nabarro–Herring creep and Coble creep have been modeled by linear viscous flows (Ashby and Verrall, 1973; Dryden et al., 1989; Yang, 1997). Note that Coble creep relies on grain boundary diffusion. Thus the application of a linear viscous constitutive equation for Coble creep is only appropriate when a representative volume element of the solid contains a large number of grains. Modern interconnects have a grain size around 100 nm and have comparable or smaller dimensions. These grains form bamboo-type lines so that the effect of Coble creep can be neglected when considering void evolution inside the grains. Dislocation core diffusion may lead to non-linear power law creep, but the mechanism acts at high deviatoric stresses. Experimental data suggest that interconnects deform elastically due to the confining effect of the surrounding passivation. In this paper we model small scale interconnects at relative high temperature due to large currents. The bulk diffusion-controlled Nabarro–Herring creep will be considered and modeled by a linear viscous constitutive equation. The study aims to reveal several key aspects of concurrent kinetics. From this point of view the result is also instructive for nonlinear creep, though the latter implies a different convective rate and will be studied in future work.

To consider diffusive interfaces we apply a modified Navier–Stokes equation with a phase field dependent surface force (Gurtin et al., 1996),

$$-\nabla p + \nabla \cdot (\eta \nabla \mathbf{v}) + \mu \nabla C = 0, \quad (2.8)$$

where  $\mathbf{v}$  is the velocity,  $\eta$  the viscosity, and  $p$  the pressure to enforce the incompressibility constraint,  $\nabla \cdot \mathbf{v} = 0$ . The viscosity is dependent on the concentration,  $\eta = \eta_0 C$ , where  $\eta_0$  is the metal viscosity. The term  $\mu \nabla C$  accounts for the force at the interface. This modified Navier–Stokes equation takes into account the hydrodynamic interaction between the concentration field and the velocity field.

Creep flow adds a convection term to the mass flux, which is given by  $C\mathbf{v}$ . In the concurrent kinetic process the net flux is the sum of this convection flux and the diffusion flux in Eq. (2.6). This combined with the mass conservation relation,  $\partial C / \partial t + \nabla \cdot \mathbf{J} = 0$ , gives a convective Cahn–Hilliard equation, namely

$$\frac{\partial C}{\partial t} + \mathbf{v} \cdot \nabla C = \nabla \cdot (M(C) \nabla \mu), \quad (2.9)$$

where  $\mu = \mu_0 - N_a |e| Z^* \phi$ .

### 3. Numerical procedure

#### 3.1. Normalization

We normalize the governing equations with a characteristic velocity  $V_c$ , length  $L_c$  and time  $t_c = L_c/V_c$ . The choice of the magnitudes of the characteristic quantities depends on the physical detail to resolve and computational convenience. The normalized equations are given by

$$\frac{\partial C}{\partial t} + \mathbf{v} \cdot \nabla C = \frac{1}{P_e} \nabla \cdot (M \nabla \mu), \quad (3.1)$$

$$\mu = 4C^3 - 6C^2 + 2C - C_h^2 \nabla^2 C - \phi, \quad (3.2)$$

$$-\nabla p + \nabla \cdot (\eta \nabla \mathbf{v}) + \frac{1}{C_a} \mu \nabla C = 0. \quad (3.3)$$

The mobility  $M$  and viscosity  $\eta$  are dimensionless numbers normalized by those of the metal,  $M_0$  and  $\eta_0$ . The potential field  $\phi$  is normalized by  $\phi_c = f_0/(N_a |e| Z^*)$ . The Péclet number,  $P_e = V_c L_c / (M_0 f_0)$ , reflects the ratio of the diffusive time scale and the convective time scale. The significance of the interface energy is described by the Cahn number,  $C_h = \sqrt{h/f_0}/L_c$ . The capillary number,  $C_a = \eta_0 V_c / (L_c f_0)$ , affects the relative magnitude of the viscous force and the interface force.

#### 3.2. Semi-implicit spectral method

Eqs. (3.1)–(3.3) and the electric field need to be solved simultaneously to obtain the evolution sequence. The coupled system requires a numerical approach with a high spatial resolution to resolve the high order derivatives in the diffusion equation. An efficient and stable time integration method should be adopted to perform three-dimensional simulations. Here we implement a semi-implicit special method, which treats the linear term implicitly and the nonlinear term explicitly to allow larger time step without losing numerical stability (Lu and Suo, 2001; Zhu et al., 1999). In contrast, fully implicit treatment yields an expensive scheme while explicit discretization quickly leads to numerical instability or needs impractical time-step constraints.

We treat the passivation and the interconnect uniformly to avoid the need to explicitly prescribe the diffusion and flow boundary conditions at the interface between the passivation and the line. The uniform treatment also enables the application of an efficient spectral method in three dimensions. We consider the passivation as part of the film, but ensure by kinetics that this part does not flow or diffuse. In other words, we assign  $M = 0$  and  $\eta \gg 1$  in the passivation region so that it keeps  $C = 1$ . In the interconnect line, according to the normalization, we have  $M = 1$  and  $\eta = 1$ . This leads to position dependent  $M$  and  $\eta$  in Eqs. (3.1) and (3.3).

To deal with the variable mobility, we rewrite the right hand side of Eq. (3.1) by

$$\nabla \cdot (M \nabla \mu) = A \nabla^2 \mu_{lr} + s_\mu, \quad (3.4)$$

where  $A$  is a constant,  $\mu_{lr}$  is a linear component of  $\mu$ , and  $s_\mu = \nabla \cdot (M \nabla \mu) - A \nabla^2 \mu_{lr}$ . The idea is to treat the linear term,  $A \nabla^2 \mu_{lr}$ , implicitly and treat the  $s_\mu$  term explicitly. This

semi-implicit approach can significantly alleviate the time step constraint. There are different choices for  $\mu_{lr}$  (Douglas and Dupont, 1971; Zhu et al., 1999). We have obtained numerical stability in all our simulations by taking  $\mu_{lr} = C - C_h^2 \nabla^2 C$  and  $A = 1$ . Note that the stability is achieved in conjunction with the extrapolated gear (SBDF) scheme for time integration. SBDF has the strongest high modal decay among the second order multi-step methods (Ascher et al., 1995). This provides the required damping for the very high frequencies in the diffusion equation without a severe time-step constraint. The convective term,  $\mathbf{v} \cdot \nabla C$ , is treated explicitly. Applying the semi-implicit method and the SBDF time integration scheme, we obtain the following discrete form for Eq. (3.1),

$$\frac{3}{2} C^{n+1} - 2C^n + \frac{1}{2} C^{n-1} = \frac{A\Delta t}{P_e} (\nabla^2 C^{n+1} - C_h^2 \nabla^4 C^{n+1}) + 2Q^n - Q^{n-1}, \quad (3.5)$$

where

$$Q^n = \frac{\Delta t}{P_e} (\nabla \cdot M \nabla \mu^n - A \nabla^2 C^n + A C_h^2 \nabla^4 C^n) - \Delta t \mathbf{v}^n \cdot \nabla C^n. \quad (3.6)$$

Eq. (3.5) can be solved with high spatial resolution efficiently in Fourier space. Applying Fourier transform to Eqs. (3.5) and (3.6), we obtain

$$\hat{C}^{n+1} = \frac{4\hat{C}^n - \hat{C}^{n-1} + 4\hat{Q}^n - 2\hat{Q}^{n-1}}{3 + (2A\Delta t/P_e)(k^2 + C_h^2 k^4)}, \quad (3.7)$$

$$\hat{Q}^n = \frac{\Delta t}{P_e} [\mathbf{i}\mathbf{k} \cdot \{M(\mathbf{i}\mathbf{k}\hat{\mu}^n)\}_{\mathbf{k}} + Ak^2 \hat{C}^n + Ak^4 C_h^2 \hat{C}^n] - \Delta t \{\mathbf{v}^n \cdot (\mathbf{i}\mathbf{k}\hat{C}^n)\}_{\mathbf{k}}, \quad (3.8)$$

where the caret ‘ $\hat{\cdot}$ ’ and the subscript  $\mathbf{k}$  stand for Fourier transform. The vector  $\mathbf{k}$  denotes the wave vector in Fourier space with  $k^2 = k_1^2 + k_2^2 + k_3^2$ . The subscript  $r$  denotes inverse Fourier transform.

The velocity field is solved by Eq. (3.3) and the incompressibility condition. To treat the variable viscosity, we rewrite

$$\nabla \cdot (\eta \nabla \mathbf{v}) = B \nabla^2 \mathbf{v} + \mathbf{r}(\mathbf{v}), \quad (3.9)$$

where  $\mathbf{r}(\mathbf{v}) = \nabla \cdot (\eta \nabla \mathbf{v}) - B \nabla^2 \mathbf{v}$  and  $B$  is a constant. We treat the linear term  $B \nabla^2 \mathbf{v}$  implicitly and the  $\mathbf{r}(\mathbf{v})$  term explicitly. Numerical stability has been achieved in all our simulations by taking  $B = \max(\eta)$ . Applying the divergence on both sides of Eq. (3.3) and substituting the incompressibility constraint  $\nabla \cdot \mathbf{v} = 0$ , we obtain the pressure at the  $n$ th time step

$$\nabla^2 p^n = \nabla \cdot \mathbf{r}(\mathbf{v}^{n-1}) + \frac{1}{C_a} \nabla \cdot (\mu^n \nabla C^n). \quad (3.10)$$

The velocity field is given by reorganizing Eq. (3.3), namely

$$\nabla^2 \mathbf{v}^n = \frac{1}{B} \left[ \nabla p^n - \mathbf{r}(\mathbf{v}^{n-1}) - \frac{1}{C_a} (\mu^n \nabla C^n) \right]. \quad (3.11)$$

The corresponding equations in Fourier space are given by

$$\hat{p}^n = -\frac{1}{k^2} \left[ \mathbf{i}\mathbf{k} \cdot \hat{\mathbf{r}}(\mathbf{v}^{n-1}) + \frac{1}{C_a} \mathbf{i}\mathbf{k} \cdot \{\mu^n (\mathbf{i}\mathbf{k}\hat{C}^n)\}_{\mathbf{k}} \right]. \quad (3.12)$$

$$\hat{\mathbf{v}}^n = -\frac{1}{Bk^2} \left[ \mathbf{i}\mathbf{k}\hat{p}^n - \hat{\mathbf{r}}(\mathbf{v}^{n-1}) - \frac{1}{C_a} \{ \mu^n (\mathbf{i}\mathbf{k}\hat{C}^n)_{\mathbf{r}} \}_{\mathbf{k}} \right]. \tag{3.13}$$

Eqs. (3.12) and (3.13) are solved iteratively.

The electric field is calculated by Eq. (2.5) with a standard second-order finite difference scheme. We adopt the preconditioned biconjugate gradient method with the Jacobi preconditioner to solve the matrix (Golub and Loan, 1989). This approach allows efficient computation of large matrices, which are typical in three-dimensional problems.

The following outlines the procedure to compute  $C^{n+1}$  from  $C^n$ . First compute the electric potential field,  $\phi^n$ , that corresponds to the concentration distribution  $C^n$ . The computed  $\phi^n$  is used to solve  $\mu^n$  by Eq. (3.2). With  $C^n$ ,  $\phi^n$ , and  $\mu^n$ , the pressure and velocity of viscous flow in Fourier space,  $\hat{p}^n$  and  $\hat{\mathbf{v}}^n$ , can be calculated by Eqs. (3.12) and (3.13). After computing  $\hat{C}^{n+1}$  with Eqs. (3.7) and (3.8), we obtain an updated concentration  $C^{n+1}$  by the inverse Fourier transform. The procedure repeats until a prescribed time.

### 3.3. Scale

Take the widely used aluminum interconnects as an example. They generally carry high electric current and operate at near half of aluminum’s melting temperature,  $T \sim 500$  K. To resolve the interface, we choose the characteristic length  $L_c$  to be  $\sqrt{h/f_0}$ . This gives  $C_h = \sqrt{h/f_0}/L_c = 1$ . The interface energy scales with  $\sqrt{hf_0} \sim 1$  J/m<sup>2</sup>. We estimate  $L_c \sim 1$  nm. This gives  $f_0 \sim 10^9$  J/m<sup>3</sup>. The characteristic time  $t_c = L_c/V_c$  is the time required for the fluid to be convected a distance on the order of the interface thickness,  $t_c = L_c/V_c \sim 10^{-5}$  s. To relate  $M_0$  to an experimentally accessible quantity, one may linearize Eqs. (3.1) and (3.2) around the equilibrium concentration (Roths et al., 2002). This gives a common diffusion equation with the corresponding diffusion coefficient being  $D = 2M_0f_0$ . Surface diffusivity of pure aluminum at a specific temperature can be estimated by  $D = 10^{-5} \exp[-0.7(\text{eV})/kT]$  m<sup>2</sup>/s, where  $k = 1.38065 \times 10^{-23}$  m<sup>2</sup>kg/s<sup>2</sup>K is Boltzmann’s constant and 1 eV = 1.6021  $\times 10^{-19}$  J (Wohlbiel, 1986). With a typical interconnect operating temperature of  $T = 500$  K, the Péclet number,  $P_e = V_c L_c / (M_0 f_0) = 2V_c L_c / D$ , is around 1–10. The effective valence of aluminum is about  $Z^* = 20$ . With  $N_a \sim 2 \times 10^{29}$  1/m<sup>3</sup>, we have  $\phi_c = f_0 / (N_a |e| Z^*) \sim 10^{-3}$  V.

To provide a rough estimation of the relative significance of surface diffusion and creep, consider a two-dimensional interconnect line in the  $x_2$ – $x_3$  plane, as shown in Fig. 2. The line has a thickness of  $H$ , with a void of radius  $R$  in the center. Due to symmetry, we only

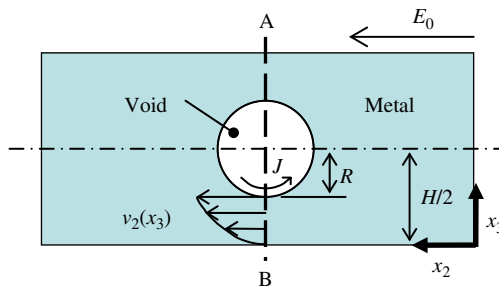


Fig. 2. Schematic of a void positioned at the center of a two-dimensional interconnect.

need to treat half of interconnect from  $x_3 = 0$  to  $x_3 = H/2$ . For simplicity we consider a steady-state condition, where the electron wind force is balanced by the pressure gradient,  $\mathbf{F}_e + \nabla p = 0$  (Blech and Herring, 1976; Suo, 2004). In the steady flow the only nonzero component of velocity is in the flux direction, and varies along the thickness, i.e.  $v_1 = v_3 = 0$  and  $v_2 = v_2(x_3)$ . Compare the amount of mass passing the dashed line A–B by creep and diffusion. With  $\partial C/\partial x_2 = 0$  and assuming a constant viscosity, Eq. (2.8) reduces to  $\eta \partial^2 v_2 / \partial x_3^2 = \partial p / \partial x_2$ . This is an ordinary differential equation for the velocity profile  $v_2(x_3)$ . Applying the no-slip boundary condition at  $x_3 = 0$  and zero shear force at the free surface,  $x_3 = H/2 - R$ , gives the velocity profile from  $x_3 = 0$  to  $x_3 = H/2 - R$ :  $v_2 = (\partial p / \partial x_2) [x_3^2/2 - (H/2 - R)x_3] / \eta$ . The mass transport by creep flow is  $Q_C = \int_0^{H/2-R} v_2 dx_3 = -(\partial p / \partial x_2) (H/2 - R)^3 / 3\eta$ , and that by surface diffusion is  $Q_D = L_c J_{x_2} = L_c M F_e$ . The ratio gives

$$\frac{Q_C}{Q_D} = \frac{H^2}{24M\eta} \left(\frac{H}{L_c}\right) \left(1 - \frac{2R}{H}\right)^3. \tag{3.14}$$

The rough estimation of Eq. (3.14) suggests that whether creep or diffusion dominates is determined by mobility, viscosity, interconnect thickness, and void radius. Fig. 3 shows that the  $Q_C = Q_D$  curve separates the space into two regions with different dominating kinetics. In both graphs a void with a radius of 10 nm is considered as an example. Fig. 3(a) shows the relation in a viscosity–temperature space for an interconnect with a thickness of 30 nm. When temperature increases a lower viscosity is needed to induce creep dominated void evolution due to enhanced mobility. The curve shows that at 500 K creep becomes important when the viscosity is below  $10^5$  Pa s. Fig. 3(b) shows the effect of film thickness, which varies from 30 nm to 1  $\mu$ m. The temperature is  $T = 500$  K. The curve suggests that the creep mechanism dominates when the interconnect thickness increases. Eq. (3.14) can be rewritten with the capillary number and Péclet number, which gives

$$\beta = \frac{Q_C}{Q_D} = \frac{1}{24} \left(\frac{H}{L_c}\right)^3 \left(1 - \frac{2R}{H}\right)^3 \left(\frac{P_e}{C_a}\right). \tag{3.15}$$

The ratio  $\beta$  is proportional to  $P_e/C_a$ . A creep dominated process corresponds to  $\beta$  much greater than 1.

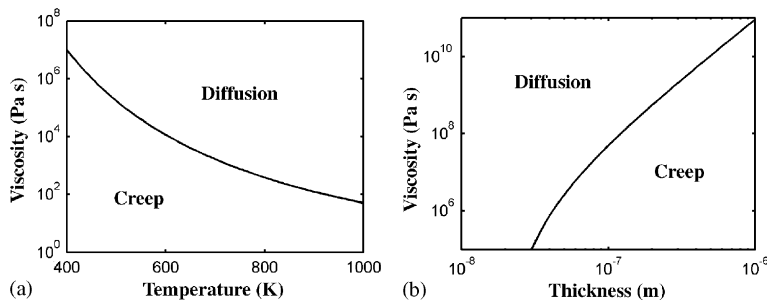


Fig. 3. Plots of dominating kinetics regions in (a) viscosity-temperature space for a 30 nm interconnect thickness, and (b) viscosity-interconnect thickness space for  $T = 500$  K.

### 4. Results and discussions

This section presents simulation results of void evolution in a three-dimensional interconnect. We aim to demonstrate how the creep mechanism, which is coupled with diffusion and electron wind, changes the void evolution in a small-scale interconnect. The Péclet number,  $P_e$ , and the capillary number,  $C_a$  are chosen based on Eq. (3.15) to consider different dominated kinetics. A thin layer in the calculation domain close to the interconnect surface is treated as the passivation. We find that assigning  $M = 0$  and  $\eta = 500$  in the passivation region is sufficient to keep it unchanged. The results are visualized by three-dimensional surface plots. The void surface is defined by the concentration of 0.5. The aluminum has a resistance of  $\rho = 2.74 \times 10^{-8} \Omega\text{m}$ . When the current is up to  $10^{12} \text{ A/m}^2$ , the electric field is around  $10^4 \text{ V/m}$ . When considering a length of  $100L_c$  (say 100 nm) the normalized electric potential is about 1.

#### 4.1. The effect of creep flow

Fig. 4 shows a comparison of three evolution sequences. The calculation domain size is  $30 \times 100 \times 30$ . A spherical void with a radius of 10 is initially positioned at (15, 15, 15). Following the previous discussions, we take the applied normalized electric potential to be 1 and the Cahn number to be  $C_h = 1$ . Eq. (3.15) gives  $\beta \sim 10P_e/C_a$ . Sequence (a) has  $P_e = 10$  and  $C_a = 10000$ , which gives  $\beta = 0.01$ . This is a diffusion dominated situation.

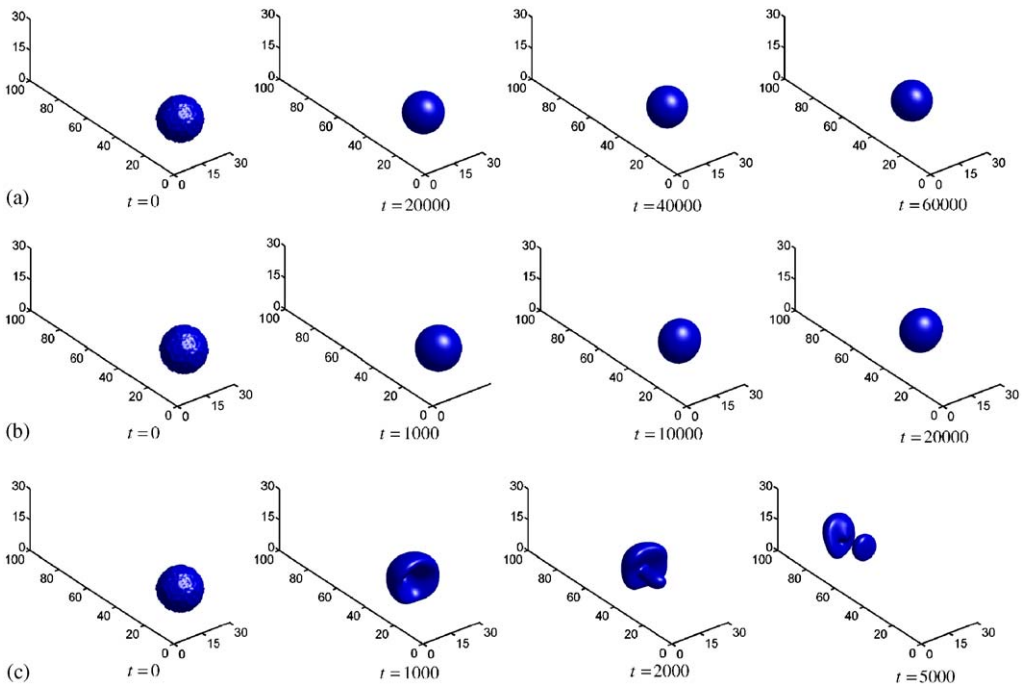


Fig. 4. A comparison of three evolution sequences with different dominating kinetics indicated by  $\beta$ . (a)  $P_e = 10$  and  $C_a = 10000$  give  $\beta = 0.01$ . Surface diffusion dominated. (b)  $P_e = 10$  and  $C_a = 100$  give  $\beta = 1$ . Comparable kinetics. (c)  $P_e = 100$  and  $C_a = 1$  give  $\beta = 1000$ . Creep dominated.

Sequence (b) has  $P_e = 10$  and  $C_a = 100$ , which gives  $\beta = 1$ . It is estimated that the effect of creep and diffusion are comparable. Sequence (c) has  $P_e = 100$  and  $C_a = 1$ , which gives  $\beta = 1000$ . This is a creep dominated situation.

The simulations show that the void migrates in the direction of the electric current, i.e. from right to left. The electron wind induces material to diffuse and flow from one side of the void to the other so that the void appears to migrate along the interconnect line. The kinetic process in Fig. 4(a) is mainly surface diffusion, where the viscosity is 100 times of that in Fig. 4(b). The high viscosity reduces any possible mass transport by creep flow. We find that the random small shape perturbation at  $t = 0$  quickly decays away. After a long evolution time,  $t = 60000$ , the void remains spherical. This is consistent with other work. Linear stability analysis has shown that subjected to an electron wind force and surface diffusion a circular void is always stable against any small shape perturbation (Mahadevan and Bradley, 1996). In other words, a stronger electric field only causes a circular void to drift faster, but does not change its shape. However, when creep exists, the situation is fundamentally different. Fig. 4(b) has already shown observable shape change. The effect is even more noticeable and interesting when creep dominates, as shown in Fig. 4(c). A spherical void evolves into a bowl shape and further breaks into two smaller voids. This dynamic process is captured from  $t = 1000$  to 5000. These simulations suggest that surface diffusion alone may not accurately account for all electromigration phenomena.

Previous studies on surface diffusion-controlled electromigration have suggested a relation between the initial void shape and its evolution. A void with an uncritical shape evolves to elongate along the interconnect line direction, while a void with a critical shape evolves to elongate normal to the line direction (Wang et al., 1996). The situation is more complicated for concurrent kinetics. Fig. 5 compares the void shape in the  $x_2$ – $x_3$  plane at  $t = 10^4$  for three cases. All the simulations start from the same spherical shape as those in Fig. 4. Fig. 5(a) is taken from the sequence in Fig. 4(b), where  $P_e = 10$  and  $C_a = 100$  give  $\beta = 1$ . Fig. 5(b) shows the case for smaller surface energy, which is half of that in Fig. 5(a),

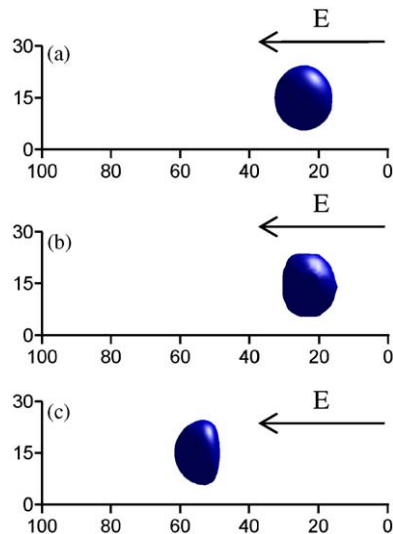


Fig. 5. Comparison of the void shape in the  $x_2$ – $x_3$  plane at  $t = 10^4$  for three cases. (a)  $\beta = 1$  ( $P_e = 10$ ,  $C_a = 100$ ),  $C_h = 1$ . (b)  $\beta = 1$  ( $P_e = 10$ ,  $C_a = 100$ ),  $C_h = 0.5$ . (c)  $\beta = 10$  ( $P_e = 10$ ,  $C_a = 10$ ),  $C_h = 1$ .

i.e.  $C_h = 0.5$ . All other parameters are the same. The void evolves to a critical shape. Fig. 5(c) shows a case with smaller viscosity, where  $P_e = 10$  and  $C_a = 10$  give  $\beta = 10$ . Other parameters are the same as those in Fig. 5(a). The void evolves to an uncritical shape. When creep becomes more prominent a bowl-shaped void appears, e.g. Fig. 4(c). Shape instability due to creep flow may eventually cause a large void to break into smaller ones.

#### 4.2. The effect of electric field strength

Two competing actions influence the void evolution: the electric field promotes the formation of slits, while the surface energy favors rounded voids. Our simulations demonstrate the same trend in the creep-dominated process. Fig. 6 shows void evolution similar to Fig. 4(c), except that a weaker electric field is applied with  $\phi = 0.5$ . The weak electron wind force leads to surface energy domination, which makes the void remain in a round shape when it migrates along the interconnect line. Fig. 7 compares two other simulations, where  $P_e = 10$  and  $C_a = 10$  give  $\beta = 10$ . The potential applied in Fig. 7(b) is  $\phi = 2$ , which is twice of that in Fig. 7(a). The strong electric field changes a round shape to the bowl shape.

#### 4.3. The effect of interconnect line thickness

Fig. 8 demonstrates the effect of interconnect geometry. The interconnect has a larger thickness compared to that in previous simulations. The calculation domain size is now  $30 \times 100 \times 50$ . The void is initially positioned at (15, 15, 25). All other parameters are the same as those in Fig. 4(c). It is observed that a thicker line leads to less flow constraint by the boundary, and the void drifts at a higher velocity. Thus the creep mechanism becomes more important in a thick line. The void shape is also affected by the interconnect geometry. While the void in Fig. 4(c) breaks into two voids in the  $x_2$  direction, the void in Fig. 8 breaks into two voids in the  $x_3$  direction. This can be understood in the following manner. The interconnect has a rectangular cross-section with a long side along the  $x_3$  axis. Face the cross-section with  $x_3$  up and imagine the mass transport occurs toward you. We can expect faster flow at regions close to the top and bottom of the void compared with the regions close to the left and right hand side of the void. This is because the top and bottom points are farther from the boundary compared to the left and right points and therefore the flow is less constrained. Then the void elongates in the  $x_3$  direction to compensate the mass flow difference. The simulations suggest that properly designing the interconnect geometry may help prevent failure due open circuits.

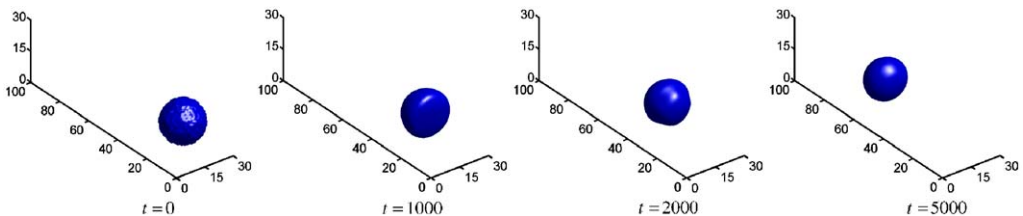


Fig. 6. An evolution similar to Fig. 4(c), except that a weaker electric field is applied,  $\phi = 0.5$ . The void remains in a round shape when it migrates along the interconnect line.

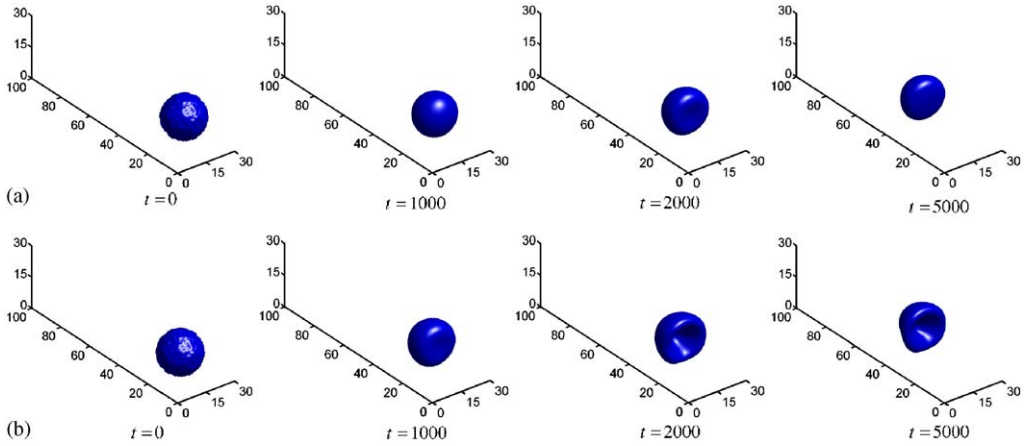


Fig. 7. The effect of electric field strength for  $P_e = 10$  and  $C_a = 10$ , which gives  $\beta = 10$ , (a)  $\phi = 1$  and (b)  $\phi = 2$ .

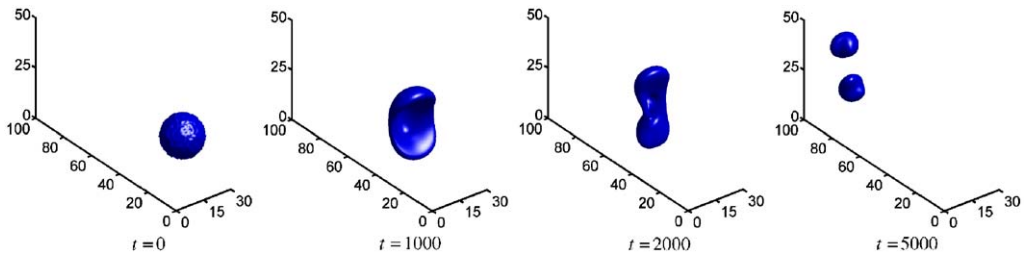


Fig. 8. Void evolution in an interconnect line with increased thickness. The domain size is  $30 \times 100 \times 50$ . All other parameters are the same as those in Fig. 4(c).

*4.4. The effect of initial void geometry*

Here, we discuss the effect of initial void geometry in a creep-dominated process, such as the initial void position and shape. Fig. 9 shows the effect of initial void position. Except for positioning the voids closer to one edge, all the parameters are the same as those in Figs. 4(c) and 8. The initial position is (15, 13, 13) in Fig. 9(a) instead of (15, 15, 15) as in Fig. 4(c), and (15, 15, 15) in Fig. 9(b) instead of (15, 15, 25) as in Fig. 8. Our three-dimensional model makes it possible to study this edge effect. The simulations show that creep flow drives a void from the initially shifted position to the centerline of an interconnect. This is presumably due to asymmetric mass transport. Consider a void shifted from the centerline. We can expect that the flow is faster on the side of the void that is further from the boundary due to less constrained flow. Then the void moves toward the centerline to compensate for the mass flow difference. Fig. 10 shows a simulation for a void with an initial ellipsoidal shape. All other parameters are the same as those in Fig. 4(c). The

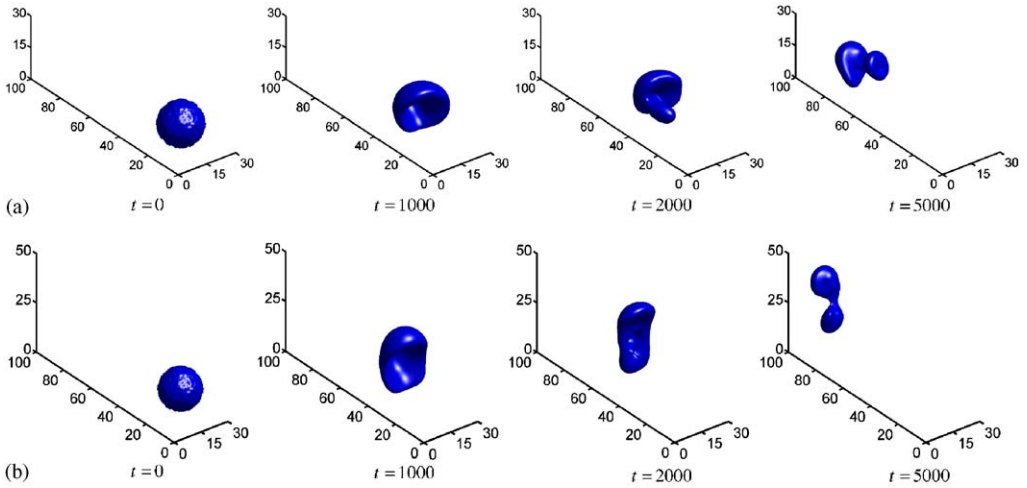


Fig. 9. The effect of initial void position. (a) The parameters are the same as those in Fig. 4(c) except that the initial void position is shifted from the center to (15, 13, 13). (b) The parameters are the same as those in Fig. 8 except that the initial void position is shifted from the center to (15, 15, 15).

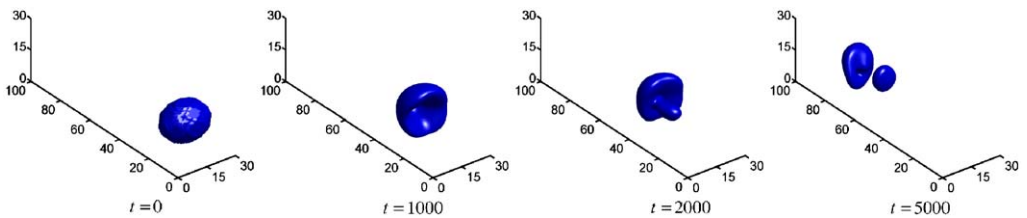


Fig. 10. A simulation for a void with an initial ellipsoidal shape. All other parameters are the same as those in Fig. 4(c).

comparison shows that the void morphologies at  $t = 5000$  are quite similar to the result shown in Fig. 4(c).

## 5. Conclusion

In a small scale interconnect both creep and diffusion contribute to the mass transport of a void. We model the coupled mechanism in electromigration in a continuum space. The three-dimensional model and computational approach proposed in this paper allow for a detailed study of the void evolution process. An approximate estimation of mass transport suggests that whether creep or diffusion dominates is determined by mobility, viscosity, interconnect thickness and void radius. The simulations show that different dominating kinetics lead to quite different morphologies. A void shape stable with surface diffusion can become unstable with creep dominated evolution. This suggests that considering the coupled mechanism may be necessary to provide reliable predictions in some situations.

## Acknowledgement

The authors acknowledge financial support from National Science Foundation Career Award No. DMI-0348375.

## References

- Arzt, E., Kraft, O., Nix, W.D., Sanchez Jr. J.E., 1994. Electromigration failure by shape change of voids in bamboo lines. *J. Appl. Phys.* 76, 1563–1571.
- Ascher, U.M., Ruuth, S.J., Wetton, B.T.R., 1995. Implicit-explicit methods for time dependent partial differential equations. *SIAM J. Numer. Anal.* 30, 797–823.
- Ashby, M.F., Verrall, R.A., 1973. Diffusion-accommodated flow and superplasticity. *Acta Metall.* 21, 149–163.
- Bhate, D.N., Kumar, A., Bower, A.F., 2000. Diffuse interface model for electromigration and stress voiding. *J. Appl. Phys.* 87 (4), 1712–1721.
- Blech, I.A., Herring, C., 1976. Stress generation by electromigration. *Appl. Phys. Lett.* 29, 131–133.
- Bower, A.F., Freund, L.B., 1993. Analysis of stress-induced void growth mechanisms in passivated interconnect lines. *J. Appl. Phys.* 74, 3855–3868.
- Cahn, J.W., 1958. Free energy of a nonuniform system. I. Interfacial free energy. *J. Chem. Phys.* 28, 258–267.
- Cho, J., Gungor, M.R., Maroudas, D., 2004. Electromigration-driven motion of morphologically stable voids in metallic thin films: Universal scaling of migration speed with void size. *Appl. Phys. Lett.* 85, 2214–2216.
- Douglas, J.J., Dupont, T., 1971. *Numerical Solution of Partial Differential Equations*. Academic Press, New York.
- Dryden, J.R., Kucerovsky, D., Wilkinson, D.S., Watt, D.F., 1989. Creep deformation due to a viscous grain boundary phase. *Acta Metall.* 37, 2007–2015.
- Fridline, D., Bower, A., 2002. Numerical simulations of stress induced void evolution and growth in interconnects. *J. Appl. Phys.* 91, 2380–2390.
- Fridline, D.R., Bower, A.F., 1999. Influence of anisotropic surface diffusivity on electromigration induced void migration and evolution. *J. Appl. Phys.* 85 (6), 3168–3174.
- Glickman, E., Osipov, N., Ivanov, A., Nathan, M., 1997. Diffusional creep as a stress relaxation mechanism in electromigration. *J. Appl. Phys.* 1998 (1), 100–107.
- Golub, G.H., Loan, C.F.V., 1989. *Matrix Computation*. Johns Hopkins University Press, Baltimore.
- Gungor, M.R., Maroudas, D., 1998. Electromigration-induced failure of metallic thin films due to transgranular void propagation. *Appl. Phys. Lett.* 72 (26), 3452–3454.
- Gungor, M.R., Maroudas, D., 1999. Theoretical analysis of electromigration-induced failure of metallic thin films due to transgranular void propagation. *J. Appl. Phys.* 85 (4), 2233–2246.
- Gurtin, M.E., Polignone, D., Viñals, J., 1996. Two-phase binary fluids and immiscible fluids described by an order parameter. *Math. Mod. Meth. Appl. Sci.* 6, 815–831.
- Kim, D., Lu, W., 2004. Self-organized nanostructures in multi-phase epilayers. *Nanotechnology* 15, 667–674.
- Kraft, O., Arzt, E., 1997. Electromigration mechanisms in conductor lines: void shape changes and slit-like failure. *Acta Mater.* 45, 1599–1611.
- Lu, W., Kim, D., 2004. Patterning nanoscale structures by surface chemistry. *Nano Lett.* 4, 313–316.
- Lu, W., Salac, D., 2005. Patterning multilayers of molecules via self-organization. *Phys. Rev. Lett.* 94, 146103.
- Lu, W., Suo, Z., 2001. Dynamics of nanoscale pattern formation of an epitaxial monolayer. *J. Mech. Phys. Solids* 49, 1937–1950.
- Mahadevan, M., Bradley, R., 1996. Stability of a circular void in a passivated, current-carrying metal film. *J. Appl. Phys.* 79, 6840–6847.
- Proost, J., Delaey, L., D’Haen, J., Maex, K., 2002. Plasticity of electromigration-induced hillocking and its effect on the critical length. *J. Appl. Phys.* 91 (11), 9108–9115.
- Roths, T., Friedrich, C., Marth, M., Honerkamp, J., 2002. Dynamics and rheology of the morphology of immiscible polymer blends—on modeling and simulation. *Rheol. Acta* 41, 211–222.
- Suo, Z., 2004. A continuum theory that couples creep and self-diffusion. *J. Appl. Mech.* 71, 646–651.
- Wang, W.Q., Suo, A., Hao, T.H., 1996. A simulation of electromigration induced transgranular slits. *J. Appl. Phys.* 79, 2394–2403.
- Wohlbiel, F.H., 1986. *Diffusion and Defect Data—Solid State Data*, vol. 47. Trans Tech, Aedermannsdorf, Switzerland.